Micro-mechanical analysis of deformation characteristics of three-dimensional granular materials

O. Durán[*] & N.P. Kruyt & S. Luding

Department of Mechanical Engineering, University of Twente, The Netherlands

April 20, 2010

Abstract

The deformation characteristics of idealized granular materials have been studied from the micro-mechanical viewpoint, using Bagi's three-dimensional micro-mechanical formulation for the strain tensor [Bagi, K. (1996), Mechanics of Materials 22: 165-177]. This formulation is based on the Delaunay tessellation of space into tetrahedra. The set of edges of the tetrahedra can be divided into physical contacts and virtual contacts between particles. Bagi's formulation expresses the continuum, macro-scale strain as an average over all edges, of their relative displacements (between two successive states) and the complementary-area vectors. This latter vector is a geometrical quantity determined from the set of edges, i.e. from the structure of the particle packing.

Results from Discrete Element Method simulations of isotropic and triaxial loading of a three-dimensional polydisperse packing of spheres have been used to investigate statistics of the branch vectors and complementary-area vectors of edges (subdivided into physical and virtual contacts) and of the relative displacements of edges. The investigated statistics are probability density functions and averages over groups of edges with the same orientation. It is shown that these averages can be represented by second-order Fourier series in edge orientation.

[*]Present address: Laboratoire de Physique et Mécanique des Milieux Hétérogènes, ESPCI, 75231 Paris Cedex, France. Email address: orencio.duran@espci.fr

Edge orientations are distributed isotropically, contrary to contact orientations. The average lengths of the branch vectors and the normal component of the complementary-area vectors are distributed isotropically (with respect to the edge orientation) and their average values are related to each other and to the volume fraction of the assembly. The other two components of the complementary-area vector are zero on average.

The total deformation of the assembly, as given by the average of the relative displacements of the edges of the Delaunay tessellation follows the uniform-strain prediction. However, neither the deformation of the physical contact network nor of the virtual contact network has this property. The average relative displacement of physical edges in the normal direction (determined by the branch vector) is smaller than that according to the uniform-strain assumption, while that of virtual contacts is larger. This is caused by the high interparticle stiffness that hinders compression. The reverse observation holds for the tangential component of the relative displacement vector. The contribution of the deformation of the empty space between physical contacts to the continuum, macro-scale strain tensor is therefore very important for the understanding and the prediction of the macro-scale deformation of granular materials.

1   Introduction

The complex mechanical behavior of granular materials during quasi-static deformation can be better understood from the micro-mechanical approach, in which relationships are studied between the macro-scale, continuum level and the micro-scale level of particles and interparticle contacts.

For quasi-static deformation of granular materials, the macro-scale, continuum quantities of interest are stress and strain. The relevant micro-scale level is that of particles and *physical contacts*, since granular materials can be idealized as assemblies of semi-rigid particles that interact at contacts through point forces. The contact forces are determined from the contact constitutive relation that involves the relative displacements of particles that are in contact.

For micro-mechanically-based constitutive relations, a so-called "localisation assumption" (see for example [Cambou et al., 1995, Liao et al., 1997, Kruyt & Rothenburg, 2002]; it also called "macro-micro assumption" or "homogenisation assumption") is required that links the

macro-scale strain to the micro-scale deformation. The proper formulation of such assumptions is an open and difficult issue. Usually, the uniform-strain assumption of affine deformation is employed. Its validity is rather limited, however [Makse et al., 1999, Kruyt & Rothenburg, 2004].

Since granular materials are generally packed randomly, the mechanical response will also show a significant random component (relative to the mean field) in contact forces and deformation. Statistical approaches are therefore considered appropriate.

Micro-mechanics of stress transmission in granular materials has been studied extensively, see for example [Bathurst & Rothenburg, 1988, Bathurst & Rothenburg, 1990, Coppersmith et al., 1996, Radjaï et al., 1996, Mueth et al., 1998, Lovøll et al., 1999, Kruyt & Rothenburg, 2001, Kruyt & Rothenburg, 2002, Kruyt, 2003a, Metzger, 2004, van Eerd et al., 2007]. On the other hand, deformation characteristics have not been studied in much detail. Most studies are restricted to the two-dimensional case [Kruyt & Rothenburg, 2003, Kruyt & Rothenburg, 2004, Kruyt & Antony, 2007, Tordesillas et al., 2010, Nguyen et al., 2009].

The focus of this micro-mechanical study is therefore on deformation characteristics of three-dimensional assemblies. A previous study [Durán et al., 2010] has shown that Bagi's micro-mechanical strain formulation [Bagi, 1996] is the most accurate three-dimensional micro-mechanical strain formulation in reconstructing the strain imposed at the boundary. Hence this formulation is employed here to study micro-mechanical characteristics of deformation.

Discrete Element Method (DEM for short) simulations [Cundall & Strack, 1979] of isotropic and triaxial loading of an initially isotropic system of spheres are used to obtain the required detailed information on particle positions and displacements, and hence on the micro-scale deformation characteristics. These two test cases are investigated, since they are frequently used to characterize the material behavior. In these DEM simulations the formation of (global) shear bands is suppressed (through the use of periodic boundary conditions) in order to obtain deformations without large-scale spatial heterogeneity.

The outline of this study is as follows. Firstly, Bagi's micro-mechanical strain formulation is summarized. Then the DEM simulations are described of isotropic and triaxial loading. The detailed results of these DEM simulations are subsequently used for the micro-mechanical analysis of the deformation characteristics.

2 Micro-mechanical strain

The strain tensor ε_{ij} is defined as the symmetrical part of the continuum-mechanical displacement gradient $\partial u_i / \partial x_j$, where $\mathbf{u}(\mathbf{x})$ is the displacement field with respect to the selected reference configuration. However, for simplicity in terminology, we will refer to the displacement gradient $\partial u_i / \partial x_j$ simply as the strain tensor:

$$\varepsilon_{ij} \equiv \frac{\partial u_i}{\partial x_j} \, . \tag{1}$$

The usual sign convention from continuum mechanics is employed, according to which compression is considered as negative.

The volume average $\bar{\varepsilon}_{ij}$ of the strain tensor over volume V, enclosed by surface S, is given by:

$$\bar{\varepsilon}_{ij} = \frac{1}{V} \int_V \varepsilon_{ij} dV = \frac{1}{V} \int_V \frac{\partial u_i}{\partial x_j} dV = \frac{1}{V} \int_S u_i n_j dS \tag{2}$$

where Gauss' divergence theorem has been used. For simplicity in notation, the overbar for the average strain $\bar{\varepsilon}_{ij}$ will be dropped in the following.

2.1 Bagi's equivalent continuum strain formulation

In this section the micro-mechanical strain tensor formulation of Bagi [Bagi, 1996] is summarized. Since this formulation is based on the Delaunay tessellation of space, this tessellation is first introduced.

2.1.1 Delaunay tessellation

The Delaunay tessellation of three-dimensional space consists of its tessellation into tetrahedra. Given a set of vertices, the tetrahedra defined by the Delaunay tessellation connect the vertices in such a way that the edges (connecting lines) of the tetrahedra form the shortest path between the vertices. An equivalent definition is that any sphere inscribed around an arbitrary tetrahedron contains no other vertex.

In a granular system the vertices of the tetrahedra are the centers of the particles and their edges correspond to the shortest path between them (see Fig. 1). An edge between particles p

and q is geometrically characterized by the branch vector $\mathbf{l}^{pq} \equiv \mathbf{X}^q - \mathbf{X}^p$ (see Fig. 2; right), where $\mathbf{X}^p$ is the position vector of the centre of mass of particle p. The subset C of all edges E, resulting from the Delaunay tessellation, that represents a *physical contact* between the particles will be simply called *contacts*. Spherical particles are in physical contact when the distance between their centers is smaller than the sum of their radii. In contrast, the other $E - C$ edges will be called *virtual contacts* (Fig. 1).
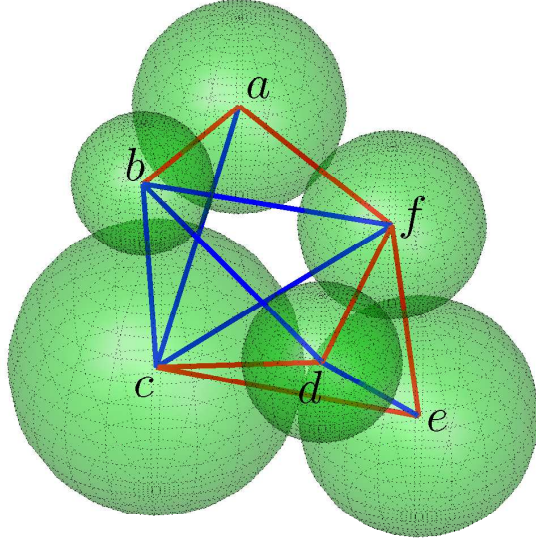

Figure 1: Delaunay tessellation of a three-dimensional granular system consisting of six spheres of different sizes. Note that the tessellation contains three tetrahedra: $\{a, b, c, f\}$, $\{b, c, d, f\}$ and $\{c, d, e, f\}$. Red edges are *physical contacts*, while blue edges indicate *virtual contacts*.

2.1.2 Strain expression

The micro-mechanical expression for the average strain tensor of a three-dimensional assembly of convex particles in a representative volume V can be written as an average over all edges of the Delaunay tessellation [Bagi, 1996]

$$\varepsilon_{ij} = \frac{1}{V} \sum_e \Delta u_i^e d_j^e = \frac{E}{V} \langle \Delta u_i d_j \rangle_e \,, \tag{3}$$

where brackets $\langle . \rangle_e$ represent the average over all E edges. Analogously, averages over physical contacts and virtual contacts are denoted by $\langle . \rangle_c$ and $\langle . \rangle_v$, respectively. The relative displacement
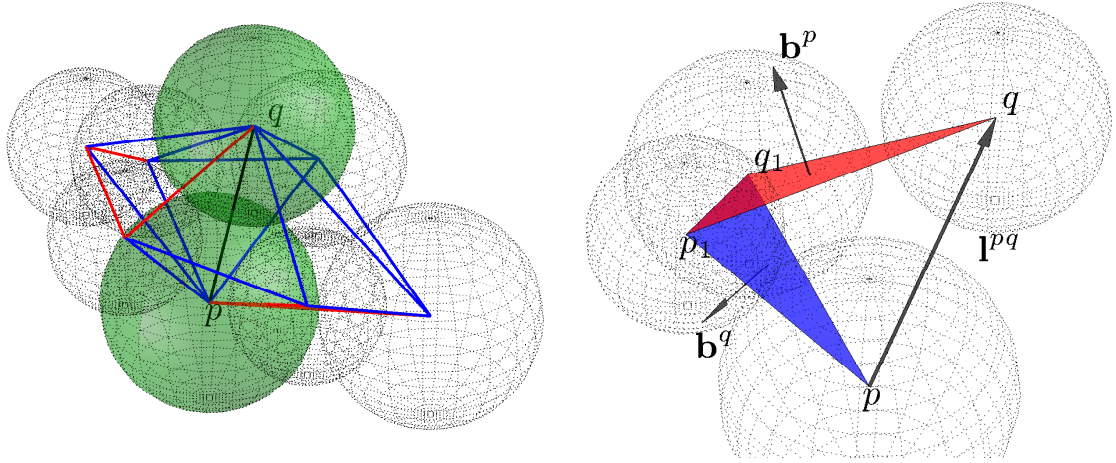
5

Figure 2: (Left) The displayed tetrahedra are formed by the particles p and q (green spheres) and the particles that are in (physical or virtual) contact with both p and q (spheres in dashed lines). Note that in this example the edge $e(p, q)$ has six neighbors and hence six tetrahedra surround it, $T_e = 6$. (Right) Branch vector $\mathbf{l}^{pq}$ connecting centers of particles p and q and area vectors $\mathbf{b}^p$ and $\mathbf{b}^q$ of the faces opposite to particle p and q, respectively, for the tetrahedron determined by the particles $\{p, q, p_1, q_1\}$ (these faces are shown in red and blue, respectively).

vector $\Delta \mathbf{u}^e$ at the edge $e(p, q)$, where index p (q) represents the particle at the *'tail'* (*'head'*) of the directed edge, respectively, is given by

$$\Delta \mathbf{u}^e = \Delta \mathbf{u}^{pq} \equiv \mathbf{U}^p - \mathbf{U}^q \, , \tag{4}$$

where $\mathbf{U}^p$ is the displacement of the centre of mass of particle p. Note that the relative displacement does not involve particle rotations.

The vector $\mathbf{d}^e$ is the complementary-area vector of the edge $e(p, q)$, defined as [Bagi, 1996]:

$$\mathbf{d}^e \equiv \frac{1}{12} \sum_{t=1}^{T_e} (\mathbf{b}^{q_t} - \mathbf{b}^{p_t}) \, , \tag{5}$$

where the sum is over all T_e tetrahedra that share the edge $e(p, q)$ (see Fig. 2; left) and the vector $\mathbf{b}^p$ represents the outward area-vector of the p face, defined as the face *opposite* to the vertex p (see Fig. 2; right). As shown in [Durán et al., 2010], $\mathbf{d}^e$ reflects the distribution of voids around a given edge e. In general, the complementary-area vector $\mathbf{d}^e$ is not parallel with the branch vector $\mathbf{l}^e$.

3   Orientational averaging

From continuum-mechanical considerations, it is expected that the relative displacement $\Delta\mathbf{u}$ of points separated by a vector $\mathbf{l}(\Omega)$, where the solid angle Ω describes the orientation of the edges between the points, is given by

$$\Delta\mathbf{u}(\Omega) = \boldsymbol{\varepsilon} \cdot \mathbf{l}(\Omega) \ . \tag{6}$$

Hence, it is meaningful to consider the average of $\Delta\mathbf{u}^e$ over groups of edges with the same orientation Ω [Rothenburg, 1980, Bathurst & Rothenburg, 1988]. Such an orientational average of an arbitrary quantity α^e associated with an edge is denoted by $\widehat{\alpha}(\Omega)$.

The orientational distribution function [Horne, 1965] of edges over a solid angle Ω is defined such that $\rho(\Omega)d\Omega$ gives the fraction of edges with orientations between Ω and $\Omega + d\Omega$. This distribution function satisfies the normalization condition $\int_\Omega \rho(\Omega)d\Omega = 1$. Corresponding orientational distribution functions for physical contacts and virtual contacts are denoted by $\rho^c(\Omega)$ and $\rho^v(\Omega)$, respectively.

The expression for the average strain tensor, Eq. (3), as a discrete sum over edges, can be transformed into a continuous form involving the orientational distribution function and the orientational average:

$$\varepsilon_{ij} = \frac{E}{V} \int_\Omega \rho(\Omega)\widehat{\Delta u_i d_j}(\Omega)d\Omega \ , \tag{7}$$

where E is the number of edges in the volume V.

The assumption that all edges individually follow the relationship $\Delta\mathbf{u}^e = \boldsymbol{\varepsilon} \cdot \mathbf{l}^e$ is called the *uniform-strain* or *affine* deformation assumption and it is often employed in micro-mechanical studies. Assuming that Eq. (6) holds is a weaker assumption of "orientational-averaged uniform strain". However, for convenience, we refer to Eq. (6) as the "uniform-strain assumption".

Relative displacements (and branch vectors) from the DEM simulations will be compared, in the following, with the prediction according to the uniform-strain assumption, Eq. (6). However, first, a local, edge-based coordinate system is defined that is convenient for representing the results in a more condensed way for the considered test cases, in particular for the triaxial compression.

3.1 Local edge-based coordinate system

In the following, triaxial and isotropic compression tests of an initially isotropic sample are considered. In the triaxial test, the deformation is imposed along the X-direction and lateral stresses are kept constant at the initial value.

The unit vector $\mathbf{n}^e = \mathbf{l}^e/||\mathbf{l}^e||$ is given by the local branch vector orientation. Using the normal vector $\mathbf{n}^e$ and one arbitrary direction unit vector $\mathbf{e}_1$, we define the unit vector $\mathbf{t}^e$ in the tangential direction and the unit vector $\mathbf{s}^e$ in the azimuthal direction. In the present study, the unit vector $\mathbf{e}_1 = \mathbf{e}_x$ along the X-direction is chosen. This is an arbitrary choice for isotropic deformation, but it is appropriate for the case of triaxial deformation.

Let $\mathbf{s}^e$ be oriented perpendicularly to the plane that contains $\mathbf{n}^e$ and $\mathbf{e}_1$. Thus $\mathbf{s}^e = (\mathbf{e}_1 \times \mathbf{n}^e)/||\mathbf{e}_1 \times \mathbf{n}^e||$ and $\mathbf{t}^e = \mathbf{s}^e \times \mathbf{n}^e$, as sketched in Fig. 3. Note that $(\mathbf{n}^e, \mathbf{t}^e, \mathbf{s}^e)$ form a local right-handed orthonormal coordinate system. Furthermore, from the definition of $\mathbf{s}^e$, when both $\mathbf{e}_1$ and $\mathbf{n}^e$ are (almost) parallel, the ratio $(\mathbf{e}_1 \times \mathbf{n}^e)/||\mathbf{e}_1 \times \mathbf{n}^e||$ remains finite, although $||\mathbf{e}_1 \times \mathbf{n}^e|| \to 0$ (see below).

Considering spherical coordinates (θ, ϕ) with symmetry axis $\mathbf{e}_1 = \mathbf{e}_x$, the polar angle θ is given by $\theta = \arccos(\mathbf{n}^e \cdot \mathbf{e}_x) \in [0, \pi]$ and the azimuthal angle $\phi \in [0, 2\pi]$. The vectors $\mathbf{n}$, $\mathbf{t}$ and $\mathbf{s}$ become:

$$\mathbf{n} = \quad \cos\theta\,\mathbf{e}_x + \cos\phi\sin\theta\,\mathbf{e}_y + \sin\phi\sin\theta\,\mathbf{e}_z \tag{8a}$$

$$\mathbf{t} = \quad -\sin\theta\,\mathbf{e}_x + \cos\phi\cos\theta\,\mathbf{e}_y + \sin\phi\cos\theta\,\mathbf{e}_z \tag{8b}$$

$$\mathbf{s} = \qquad\qquad -\sin\phi\,\mathbf{e}_y + \cos\phi\,\mathbf{e}_z \tag{8c}$$

where the superscript e, denoting a given edge, is dropped since, the angles (θ, ϕ) correspond not to a single edge, but to a family of edges.

In this local coordinate system any vector $\mathbf{A}$ associated with an edge (such as the relative displacement vectors $\Delta\mathbf{u}^e$, the branch vector $\mathbf{l}^e$ and the complementary-area vectors $\mathbf{d}^e$) can be decomposed as

$$\mathbf{A} = A_n\mathbf{n} + A_t\mathbf{t} + A_s\mathbf{s} . \tag{9}$$

For the triaxial compression test the boundary conditions for the representative volume V
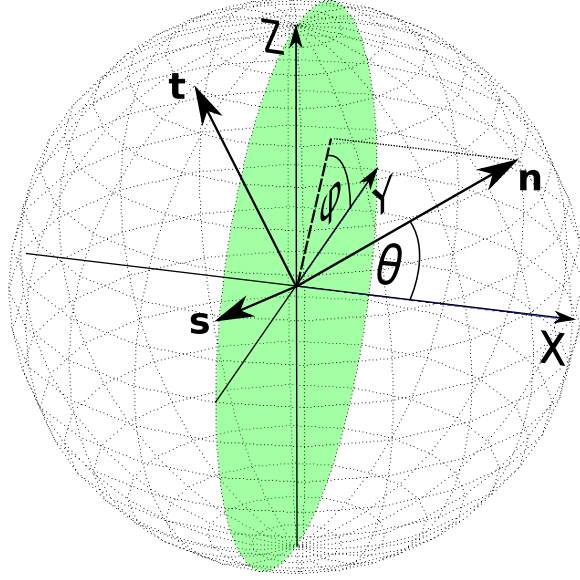
Figure 3: Sketch of the local, edge-based coordinate system $(\mathbf{n}, \mathbf{t}, \mathbf{s})$ for an edge that is oriented along $\mathbf{n}$. The Cartesian coordinate system (x, y, z), a sphere with unit radius and the azimuthal and polar angles, θ and ϕ, respectively, are shown for reference. Note that by definition the vectors $(\mathbf{n}, \mathbf{t})$ are coplanar with $\mathbf{e}_x$, while $\mathbf{s}$ is in the plane $y - z$ (green region).

are symmetrical in the Y, Z plane (the azimuthal plane). Given this polar (cylindrical) symmetry around the X-axis, it is expected that the *orientational average* (over edges with similar orientations) of an edge quantity A (denoted by $\widehat{A}(\Omega)$, or in terms of angles (θ, ϕ) by $\widehat{A}(\theta, \phi)$) is independent of ϕ. Then only the *azimuthal average* (or polar average), denoted by $\overline{A}(\theta)$, is important. This reduction forms the main motivation for the introduction of the local, edge-based coordinate system.

Notice that an edge pq is equivalent to the edge qp. The orientation of edge pq is expressed by the spherical coordinates (θ, ϕ). The orientation of edge qp then is given by $(\pi - \theta, \pi - \phi)$. Therefore, the orientational average satisfies $\widehat{A}(\pi - \theta, \pi - \phi) = \widehat{A}(\theta, \phi)$ and the azimuthal average satisfies $\overline{A}(\pi - \theta) = \overline{A}(\theta)$.

The orientational distribution function $\rho(\theta, \phi)$ will (also) only depend on θ for the considered test cases. The corresponding (polar) distribution is denoted by $\rho_\theta(\theta)$. A similar meaning is implied by $\rho_\theta^c(\theta)$ and $\rho_\theta^v(\theta)$.

3.2 Uniform strain

Here the azimuthally-averaged relative displacement vector according to the uniform-strain assumption Eq. (6) is given for a triaxial test. This relative displacement vector is expressed in the components $\{\widetilde{\Delta u_n}, \widetilde{\Delta u_t}, \widetilde{\Delta u_s}\}$ (compare Eq. (9)). Here, and in the following, the tilde indicates quantities that are obtained from the uniform-strain assumption. As shown in the Appendix, these components are given by

$$\widetilde{\Delta u_n}(\theta) = \langle l \rangle \left[\left(\frac{\varepsilon_{11} + \varepsilon_{22}}{2} \right) + \left(\frac{\varepsilon_{11} - \varepsilon_{22}}{2} \right) \cos 2\theta \right] \tag{10a}$$

$$\widetilde{\Delta u_t}(\theta) = -\langle l \rangle \left[\left(\frac{\varepsilon_{11} - \varepsilon_{22}}{2} \right) \sin 2\theta \right] \tag{10b}$$

$$\widetilde{\Delta u_s}(\theta) = 0 \tag{10c}$$

or, in terms of the Fourier components $\tilde{a}_0$, $\tilde{a}_n$, $\tilde{a}_t$

$$\widetilde{\Delta u_n}(\theta) = \langle l \rangle \left(\tilde{a}_0 + \tilde{a}_n \cos 2\theta \right) \tag{11a}$$

$$\widetilde{\Delta u_t}(\theta) = -\langle l \rangle \tilde{a}_t \sin 2\theta \tag{11b}$$

where

$$\tilde{a}_0 = \frac{\varepsilon_{11} + \varepsilon_{22}}{2} \tag{12a}$$

$$\tilde{a}_n = \frac{\varepsilon_{11} - \varepsilon_{22}}{2} \tag{12b}$$

$$\tilde{a}_t = \tilde{a}_n \tag{12c}$$

The results for the (azimuthally-averaged) components $\{\overline{\Delta u_n}(\theta), \overline{\Delta u_t}(\theta)\}$ of the relative displacements from the DEM simulations, described in the next section, conform to Eq. (11), but the corresponding coefficients a_0, a_n and a_t differ from those given in Eq. (12). Therefore, the deviations from the ideal case of uniform-strain (or affine) deformation can be characterized by the ratio between the actual Fourier coefficients ($a_{0,n,t}$) for the relative displacements of edges, contacts or virtual contacts, and those predicted by the uniform-strain assumption ($\tilde{a}_{0,n,t}$), i.e. by the set of coefficients γ_0, γ_n and γ_t, defined by

$$\gamma_{0,n,t} \equiv \frac{a_{0,n,t}}{\tilde{a}_{0,n,t}} , \tag{13}$$

Results for these coefficients are presented in Section 5.3.

10

4   Discrete Element Method simulations

Discrete Element Method (DEM) simulations, as proposed by [Cundall & Strack, 1979], have been performed to obtain detailed information on particle displacements (and hence relative displacements at the edges) under triaxial and isotropic compressive loading conditions.

The assembly consists of 250,000 polydisperse spherical particles, with radii from a log-normal distribution. Its standard deviation is 0.25, relative to the mean particle radius $\langle r \rangle$. The initial, isotropic packing is prepared under isotropic stress conditions, with stress σ_0 and with particle friction switched off, i.e. the interparticle friction coefficient $\mu = 0$. Its volume fraction ν, i.e. the volume occupied by the particles divided by the total assembly volume (including voids), is 0.65 and the (physical) coordination number C_c (the average number of physical contacts per particle) is $C_c = 6.19$. The length of the initial cubic assembly is about 60 times the average particle diameter.

The contact constitutive relation of [Cundall & Strack, 1979] is used, in which the elastic parts of the contact constitutive relations, for the normal and tangential contact forces, are linear. The stiffness ratio $k_t/k_n = 0.5$, with k_n and k_t being the stiffnesses in normal and tangential directions, respectively. The interparticle friction coefficient $\mu = 0.5$. The contact deformations ('overlaps') are small, since the non-dimensional stress $\sigma_0 \langle r \rangle / k_n \approx 10^{-3}$ is small.

For the triaxial loading the compressive displacement is imposed in the X-direction, while the lateral deformation is such that the lateral stresses are kept constant at the initial stress σ_0. Periodic boundary conditions have been employed to avoid wall effects and to suppress the formations of (global) shear bands so that large deformations without large-scale heterogeneity can be studied. Note that small-scale heterogeneities will always be present [Kuhn, 1999].

The macro-scale deformation of the periodic box is determined from the deformation of the periodic box, with lengths L_i and initial lengths L_i^0

$$e_{ij} \;=\; \ln \frac{L_i}{L_i^0} \, \delta_{ij} \;. \tag{14}$$

In the triaxial test the principal-strain directions correspond to the Cartesian coordinate system for the periodic box. Note that the tensor e represents the cumulative deformation given by $e \equiv \int_{L^0}^{L} \varepsilon$, where ε is the incremental strain tensor.

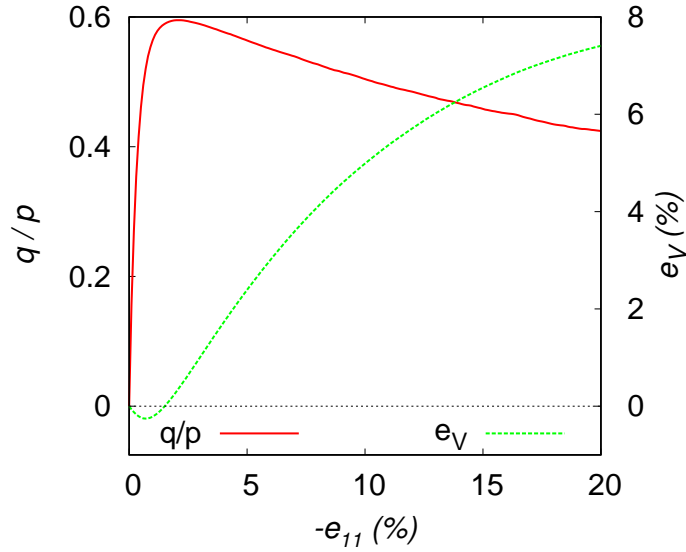The macro-scale, continuum response is characterized by the deviatoric stress ratio q/p with

Figure 4: Evolution of the total volumetric strain e_V and the ratio of the deviatoric stress ratio q/p (as defined in the main text) as a function of the total axial deformation $-e_{11}$, where compression is considered negative.

invariant $q = (\sigma_{11} - \sigma_{22})/2$ of the deviatoric stress and pressure $p = \operatorname{tr} \boldsymbol{\sigma}/3$ and volumetric strain e_V ($e_V \equiv \operatorname{tr} \boldsymbol{e} = \ln V/V_0$, where V is the volume of the current state and V_0 is the volume of the initial state). Figure 4 shows the evolution, as function of the total imposed axial deformation e_{11}, of the deviatoric stress ratio and volumetric strain, with the characteristic compression-dilation behavior for a dense initial packing. The yield stress is reached after about 2% of axial deformation. Note that no (global) shear band was observed, due to the use of periodic boundary conditions.

In a previous study [Durán et al., 2010] it has been shown that Bagi's micro-mechanical expression, Eq. (3), for the average strain tensor accurately represents the macro-scale deformation of the boundaries, i.e. the changing lengths of the periodic box.

The employed Delaunay tessellation procedure does not take into account the periodic boundaries of the system. Hence only "internal" tetrahedra are employed. These internal tetrahedra are located more than 5% of the system size away from any of the periodic boundaries.

5 Results

In this section, we study the evolution of the deformation characteristics with imposed loading, as well as the geometrical quantities involved in Bagi's strain formulation. Hence, we will consider the evolution of branch vectors $\mathbf{l}^e$ and the complementary-area vectors $\mathbf{d}^e$, and their orientational averages.

Furthermore, we will also study the probability distribution function (PDF) and the evolution of the polar distribution of the components $\{\overline{\Delta u_n}(\theta), \overline{\Delta u_t}(\theta), \overline{\Delta u_s}(\theta)\}$ of the azimuthally-averaged relative displacements from the DEM simulations. Although the geometrical quantities will be mainly studied for triaxial loading, we will also show some results for isotropic loading, whenever they show interesting behavior.

5.1 Geometry

Due to their relevance for Bagi's strain formulation, see Eq. (3), we will study in detail the geometrical quantities:

- edge-based and contact-based coordination numbers C_e and C_c, respectively;

- the edge structure, i.e. the polar distribution of edges $\rho_\theta(\theta)$, contacts $\rho_\theta^c(\theta)$ and virtual contacts $\rho_\theta^v(\theta)$ (see Section 3.1);

- geometrical quantities like the azimuthally-averaged branch vectors of edges $\bar{l}(\theta)$, contacts $\overline{l^c}(\theta)$ and virtual contacts $\overline{l^v}(\theta)$, as well as the components of the complementary-area vector $\overline{\mathbf{d}}(\theta)$ for edges, contacts and virtual contacts.

5.1.1 Coordination numbers

The connectivity of the packing and the Delaunay tessellation is primarily described by the contact-based and edge-based coordination numbers C_c and C_e, respectively, defined as

$$C_c = 2C/N \tag{15}$$
$$C_e = 2E/N \tag{16}$$

where C, E and N are the number of (physical) contacts, edges and particles, respectively. These coordination numbers C_c and C_e give the average number of contacts and edges per particle, respectively.

The coordination number of the Delaunay tessellation C_e remains roughly constant during the tests (with a slight increase of about 2% for the triaxial test and less than one percent decrease for isotropic compression): $C_e \approx 14.3 - 14.5$, while C_c decreases (increases) by about 30% for triaxial (isotropic) compression, see Fig. 5 (left).
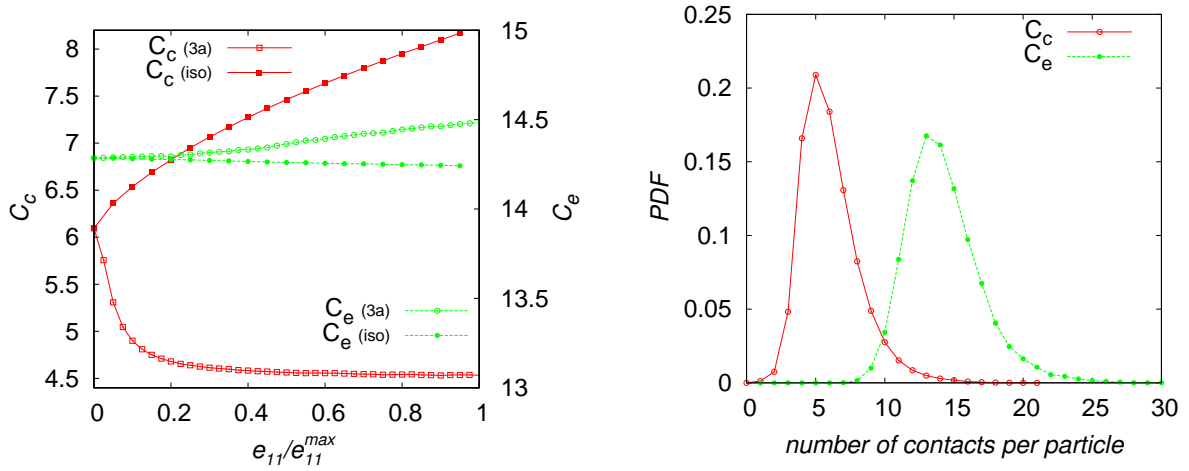
Figure 5: (Left) Evolution of the coordination numbers of edges C_e and contacts C_c during the isotropic (iso) and triaxial (3a) compression test. The axial deformation is normalized by its maximum value $e_{11}^{max} = -20\%$ and -5% for the triaxial and isotropic compression, respectively. (Right) Probability density function of C_e and C_c in the initial isotropic state.

Figure 5 (right) shows the probability density function of C_e and C_c in the initial isotropic state, as also studied, e.g. by [Lochmann et al., 2006].

Rattlers (i.e. particles without physical contacts) are ignored in the analyses, so there are no particles with $C = 0$, while there are few particles with less than three contacts. We furthermore observe few particles with less than 8 edges, but most have many more edges with an average of $C_e \approx 14.3$.

5.1.2 Distribution of edge and contact orientations

Figure 6 shows the distribution of the edge orientations $\rho(\Omega)$ and contact orientations $\rho^c(\Omega)$, for the triaxial test. It is clear that they are independent of azimuthal angle ϕ, as expected in the considered triaxial test with its transverse symmetry (see also Section 3.1). Therefore, only the distribution $\rho_\theta(\theta)$ contains relevant information.
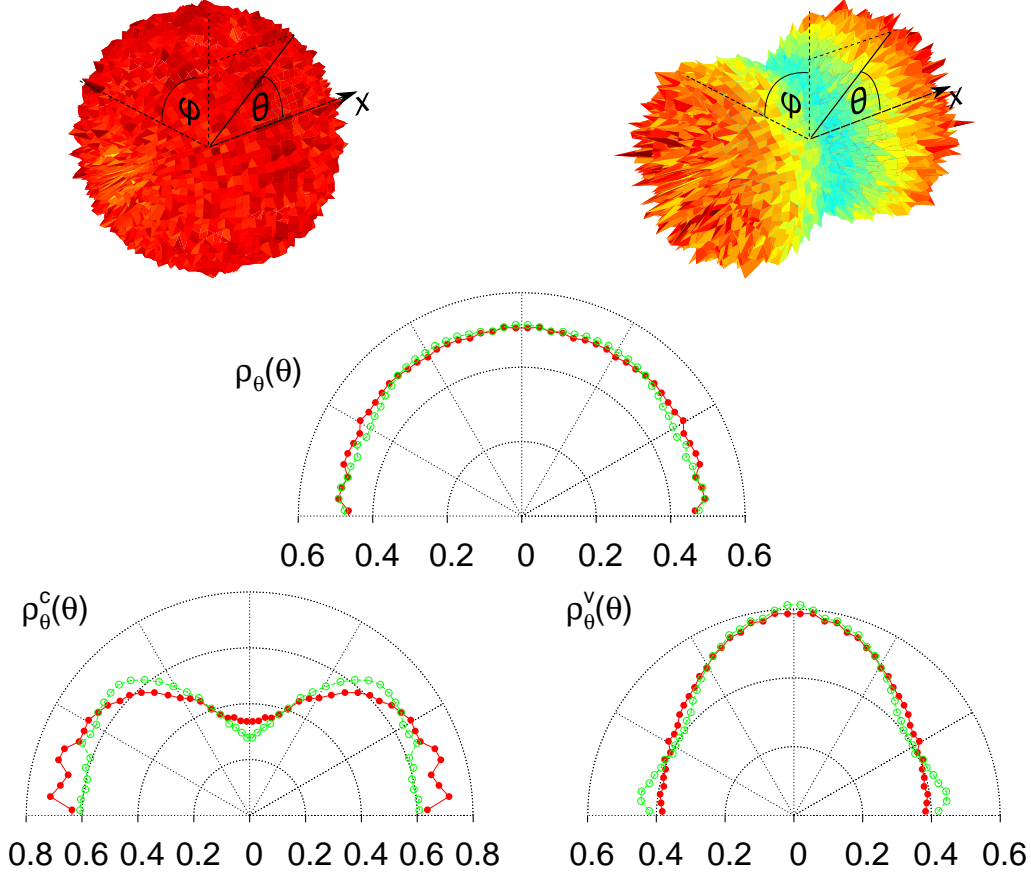

Figure 6: (Top) Orientational distribution of edges (left) and contacts (right) at peak shear strength ratio, $e_{11} = -2\%$ from the triaxial test. (Bottom) Plot of the polar distribution of edges $\rho_\theta(\theta)$ (top), contacts $\rho_\theta^c(\theta)$ and virtual contacts $\rho_\theta^v(\theta)$ (bottom left and right, respectively), at $e_{11} = -2\%$ (solid symbols, in red), and for large deformations, $e_{11} = -20\%$ (open symbols, in green), where θ is the polar angle, with $\theta \in [0, \pi]$ by definition.

The distribution of the edge orientation $\rho(\Omega)$ is isotropic during the whole deformation, as was already observed in the two-dimensional case [Tordesillas et al., 2010]. In contrast, the polar distribution of contacts $\rho_\theta^c(\theta)$ (see Fig. 6, bottom left) is highly anisotropic during the

triaxial test. Along the compression axis ($\theta = 0$) contacts are created ($\rho_\theta^c(\theta) > 1/2$), while in the directions of minor principal stresses ($\theta = \pi/2$) contacts are disrupted ($\rho_\theta^c(\theta) < 1/2$). Note that the distribution of virtual contacts $\rho_\theta^v(\theta)$ (Fig. 6, bottom right) is not independent and can be calculated from:

$$\rho_\theta(\theta) = n_C \, \rho_\theta^c(\theta) + (1 - n_C) \, \rho_\theta^v(\theta) \,, \tag{17}$$

where n_C is the fraction of edges that are (physical) contacts. This fraction can be expressed in terms of the coordination numbers C_c and C_e (defined in Eqs. (15) and (16)):

$$n_C \equiv \frac{C}{E} = \frac{C_c}{C_e} \,. \tag{18}$$

In our simulations the value of n_C varies from $\sim 0.3 - 0.5$.

In order to study the evolution of the structure, i.e. the polar distribution of edges and contacts $\rho_\theta(\theta)$ and $\rho_\theta^c(\theta)$, in compact terms, we decompose them in Fourier series in θ:

$$\rho_\theta(\theta) \approx \rho_0 + \rho_2 \cos 2\theta + \rho_4 \cos 4\theta + ... \tag{19}$$

$$\rho_\theta^c(\theta) \approx \rho_0^c + \rho_2^c \cos 2\theta + \rho_4^c \cos 4\theta + ... \tag{20}$$

and study the evolution of the Fourier components ρ_i and ρ_i^c, for $i = 0, 2, 4$. The coefficients $\rho_{2,4}$ and $\rho_{2,4}^c$ reflect the anisotropy of the structure. Note that odd terms, like $\cos \theta$, are not present due to symmetry reasons, i.e. the distributions are periodic in the interval $\theta \in [0, \pi]$. Higher order terms were practically zero in the cases tested, so that we restrict ourselves to $i = 0, 2$, and 4. From the normalization condition for distribution functions, $\int_\Omega \rho(\Omega) d\Omega = 1$, we then find that $\rho_0 = 1/2 + \rho_2/3 + \rho_4/15$.

The evolution during the triaxial test of these Fourier coefficients is shown in Fig. 7. As is shown in Fig. 7 (left) for the edge distribution, the anisotropy coefficients ρ_2 and ρ_4 are small compared to the isotropic one ρ_0, which confirms the isotropic character of the Delaunay edge network: an isotropic network would correspond to $\rho_0 \equiv 1/2$ and $\rho_2 = \rho_4 \equiv 0$. On the contrary, the contact network is highly anisotropic. As implied by Fig. 7 (right), both anisotropy coefficients, ρ_2^c and ρ_4^c, increase with the deformation e_{11}. In particular, for large deformations ($|e_{11}| > 10\%$), the higher order Fourier component ρ_4^c becomes as relevant as ρ_2^c.
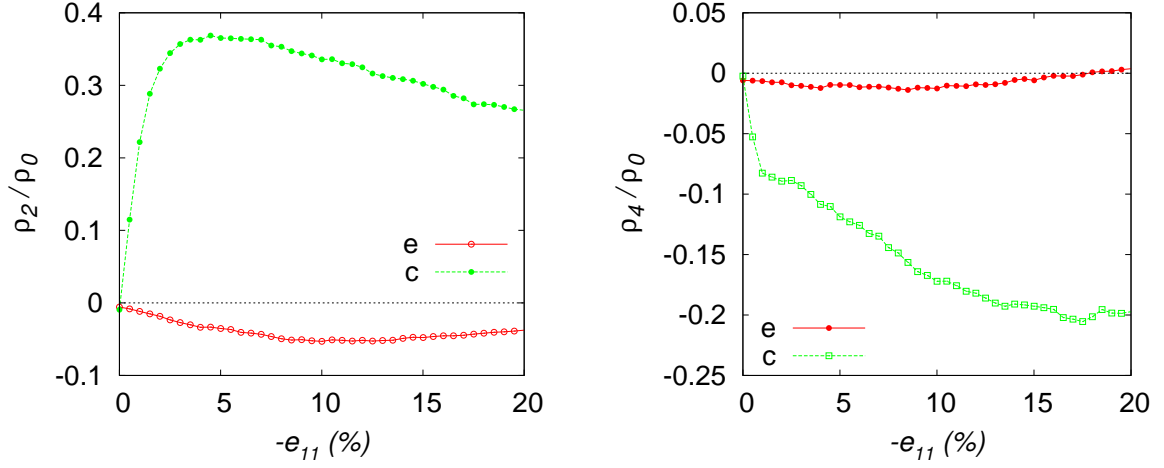
Figure 7: (Left) Evolution of the second-order Fourier components, relative to the isotropic value, of the polar distribution function of edges $\rho_\theta(\theta)$ and contacts $\rho_\theta^c(\theta)$. (Right) Evolution of the fourth-order Fourier components, relative to the isotropic value, of the polar distribution functions of edges and contacts.

5.1.3 Characteristics of branch length and complementary-area vector

In this section the characteristics of the branch vector and the complementary-area vector are given. This involves the polar distribution, as well as the evolution in the triaxial test of the Fourier components for the average values.

Branch length

After azimuthal averaging (see Section 3.1), the lengths of edges and contacts, $\overline{l^e}(\theta)$ and $\overline{l^c}(\theta)$, respectively, are approximately isotropic during the whole triaxial test. This is a consequence of the statistically uniform spatial distribution of particles, and thus edges, in the random packings.

Figure 8 shows the evolution of the average length of the branch vectors $\langle l \rangle_{e,c,v}$ for edges, contacts and virtual contacts. The evolution of the average edge length closely resembles the volumetric deformation of the assembly (see Fig. 4). Since the total volume of the particles is conserved, the volume fraction should scale as $\nu \propto \langle r \rangle^3 / \langle l \rangle_e^3$, where $\langle r \rangle$ is the mean particle radius and $\langle l \rangle_e$ represents an average distance between particles, based on the definition of the Delaunay tessellation. Therefore $\langle l \rangle_e$ is proportional to $\langle r \rangle / \sqrt[3]{\nu}$ (as shown by the solid line in
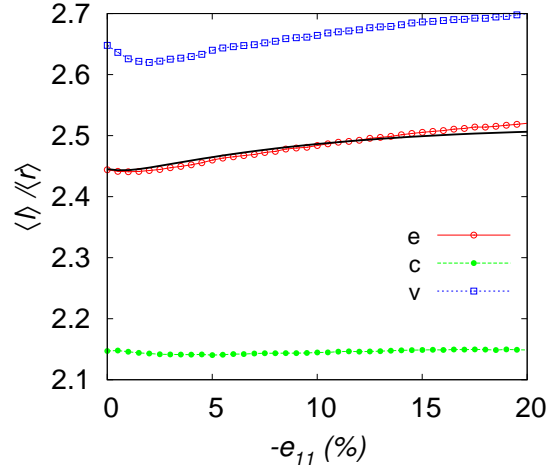
17

Figure 8: Evolution of the dimensionless average branch vector length $\langle l \rangle / \langle r \rangle$, where $\langle r \rangle$ is the mean particle radius, for edges (e), contacts (c) and virtual contacts (v). The dimensionless length $1/\sqrt[3]{\nu}$ (solid line), based on the volume fraction ν, is also shown for comparison.

Fig. 8, with a single proportionality constant that is determined by matching the initial value at e_{11}).

As expected for a low confining pressure (relative to the particle stiffness k_n), the macro-scale deformation of the assembly does not significantly affect the average length of (physical) contacts $\langle l \rangle_c$, which remains nearly constant during the whole test. In contrast, larger deformations occur in the empty space between the particles, encoded in $\langle l \rangle_v$.

Finally, note that for contacts $\langle l \rangle_c / \langle r \rangle > 2$ (Fig. 8). This is a direct consequence of the polydispersity of the assembly and has its origin in the correlation between the particle radius and the number of contacts of a given particle: large particles with large surface area have more contacts than small particles [Kruyt & Rothenburg, 2001, Madadi et al., 2004, Durán & Luding, 2010].

Complementary-area vector

For the complementary-area vector $\mathbf{d}^e$, only the normal component $\overline{d_n}(\theta)$ is different from zero after azimuthal averaging, due to the statistical uniformity of the random packing. Thus, even though the individual complementary-area vectors $\mathbf{d}^e$ are not parallel to the branch vectors $\mathbf{l}^e$,

azimuthally-averaged they are parallel.

The azimuthally-averaged normal component of the complementary-area vector $\overline{d_n}(\theta)$ can (also) be expressed as a Fourier series in the polar angle θ: $\overline{d_n}(\theta) \approx d_{n0} + d_{n2}\cos 2\theta$. The analysis of the anisotropy ratio d_{n2}/d_{n0} (Fig. 9, left) shows that the normal complementary area $\overline{d_n}(\theta)$ is nearly isotropic for edges and contacts ($|d_{n2}/d_{n0}| < 2\%$), while for virtual contacts it becomes slightly anisotropic for large deformations ($d_{n2}/d_{n0} \sim -10\%$), where a negative value means that the complementary-area vectors are somewhat smaller in the compression direction than in the extension direction. The even smaller coefficient of the fourth-order harmonic is not shown and discussed here.
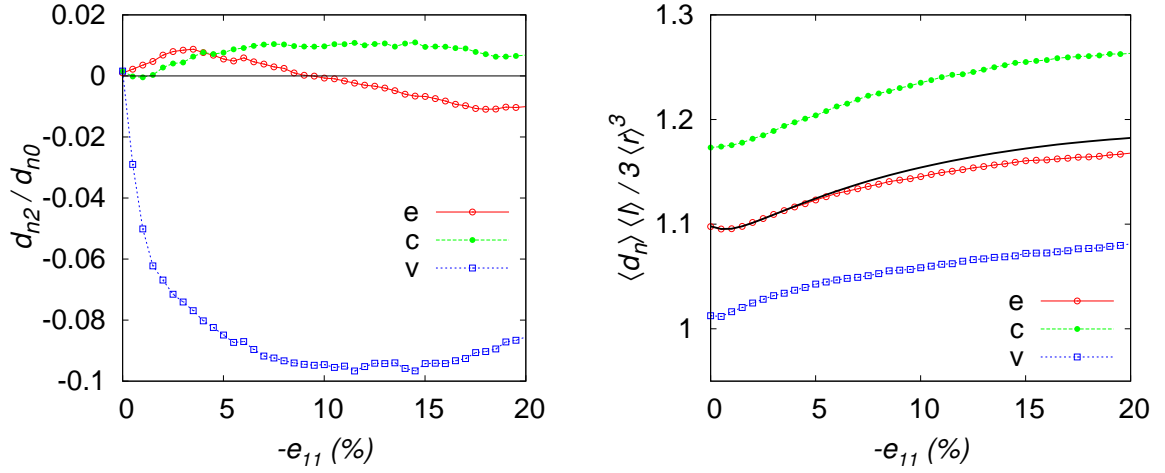

Figure 9: Normal component d_n of the complementary-area vector for edges (e), contacts (c) and virtual contacts (v) in triaxial test. (Left) Evolution of the anisotropy ratio d_{n2}/d_{n0} (Right) Evolution of the normalized average $\langle d_n\rangle\langle l\rangle/(3\langle r\rangle^3)$. As shown by the solid line in the right panel, $\langle d_n\rangle_e\langle l\rangle_e/(3\langle r\rangle^3)$ is proportional to the inverse of the volume fraction $1/\nu$.

The evolution of the normalized average $\langle d_n\rangle_{e,c,v}\langle l\rangle_{e,c,v}/(3\langle r\rangle^3)$ is shown in Fig. 9 (right) for edges, contacts and virtual contacts. The scaling of $\langle d_n\rangle_e$ with $3\langle r\rangle^3/\langle l\rangle_e$, where $\langle r\rangle$ is the mean particle radius, is suggested by the geometrical identity [Durán et al., 2010]

$$\langle d_n l\rangle_e = 3V/E , \tag{21}$$

which implies an additional relation with the volume fraction ν. Since the number of edges remains almost constant during the test (see Fig. 5, left) and the actual volume of the packing

19

is proportional to $\langle r \rangle^3/\nu$, it follows that $\langle d_n \rangle_e \langle l \rangle_e / (3\langle r \rangle^3) \propto 1/\nu$, as shown by the solid line in Fig. 9 (right). The single proportionality constant has been set to match the initial value at $e_{11} = 0$.

5.2 Relative displacements

In this section we study the relative displacements of edges, (physical) contacts and virtual contacts during triaxial and isotropic loading. In particular, we will focus on the orientational averages and the probability distribution function (PDF) of the normal and tangential components of the relative displacements for edges, contacts and virtual contacts.

The orientationally-averaged components of the relative displacement vector, $\widehat{\Delta u_n}(\theta, \phi)$, $\widehat{\Delta u_t}(\theta, \phi)$ and $\widehat{\Delta u_s}(\theta, \phi)$, are shown in Fig. 10 for the triaxial test. As expected due to the polar symmetry (see also Section 3.1), these averages are independent of ϕ and the out-of-plane component vanishes, $\widehat{\Delta u_s}(\theta, \phi) \approx 0$.
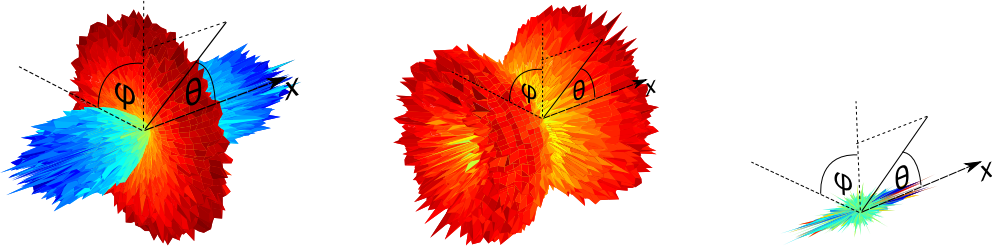

Figure 10: Orientational averages $\widehat{\Delta u_n}(\theta, \phi)$, $\widehat{\Delta u_t}(\theta, \phi)$ and $\widehat{\Delta u_s}(\theta, \phi)$ for edges for triaxial loading at deformation $e_{11} = -2\%$. The magnitude of the average is given by the color code, where red represents positive values and blue negative values. Note that $\widehat{\Delta u_s}$ is negligible.

In the following, we will therefore study the azimuthally-averaged normal and tangential component of the relative displacement of edges $\overline{\Delta u}_{n,t}^{\,e}(\theta)$ by analyzing the behavior of the contact $\overline{\Delta u}_{n,t}^{\,c}(\theta)$ and virtual contact $\overline{\Delta u}_{n,t}^{\,v}(\theta)$ contributions separately. These components are not independent, as they are related by the normalization condition:

$$\rho_\theta(\theta)\overline{\Delta u}_{n,t}^{\,e}(\theta) = n_C \rho_\theta^c(\theta)\overline{\Delta u}_{n,t}^{\,c}(\theta) + (1 - n_C)\rho_\theta^v(\theta)\overline{\Delta u}_{n,t}^{\,v}(\theta) , \tag{22}$$

where $\rho_\theta(\theta)$ and n_C are defined in Eqs. (17) and (18), respectively.

5.2.1 Normal component
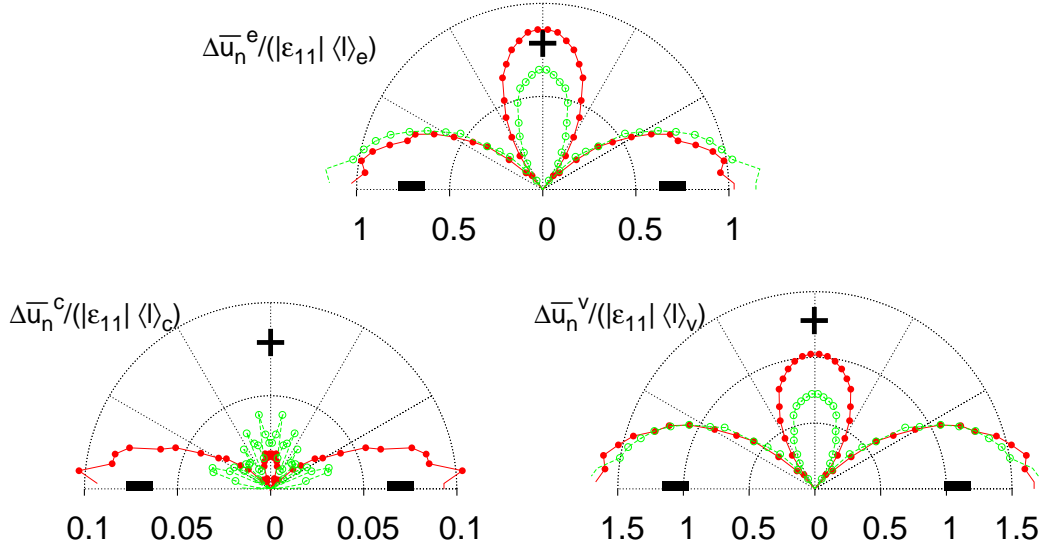
Figure 11 shows the polar distribution of the normal components of the azimuthally-averaged relative displacements $\overline{\Delta u}_n^{e,c,v}(\theta)/(|\varepsilon_{11}|\langle l\rangle_{e,c,v})$ for edges, contacts and virtual contacts, at two different axial deformations e_{11} during the triaxial test. The relative displacements of edges, contacts, and virtual contacts are normalized by the respective average length of the branch vectors and by the strain increment $|\varepsilon_{11}|$.

Figure 11: Triaxial loading: polar distribution of the scaled normal components of the azimuthally-averaged relative displacements $\overline{\Delta u_n}(\theta)/(|\varepsilon_{11}|\langle l\rangle)$ for edges (top), contacts and virtual contacts (bottom left and right, respectively) at $e_{11} = -2\%$ (full symbols in red) and -20% (open symbols in green). Negative $(-)$ and positive $(+)$ labels indicate compression and extension, respectively.

As expected for triaxial compression, edges are compressed ($\overline{\Delta u}_n^e < 0$) in the X-axis ($\theta = 0$), while they expand ($\overline{\Delta u}_n^e > 0$) in the extension direction ($\theta = \pi/2$), see Fig. 11. However, this significantly changes when the deformation of contacts and virtual contacts is analyzed separately. Although virtual contacts deform (in the normal direction) in a way similar to that of edges, they are deformed more. On the other hand, contacts are only slightly compressed due to the strong repulsive forces active. For large deformations ($e_{11} \sim -20\%$), they practically do not deform at all in the contact direction, i.e. $\overline{\Delta u}_n^c \sim 0$ (Fig. 11, left). In this regime, the

deformation in the normal direction occurs predominantly in the space between particles, i.e. 'deformation of voids' (characterized by the virtual contacts).

In general, the compressive (considered as negative) response in relative displacements is stronger than the extension (considered as positive) one. This observation is true for the peak stress (red) and – even stronger – for the large strain regime (green). The contacts have no significant (average) relative displacement in the large strain regime in any direction.
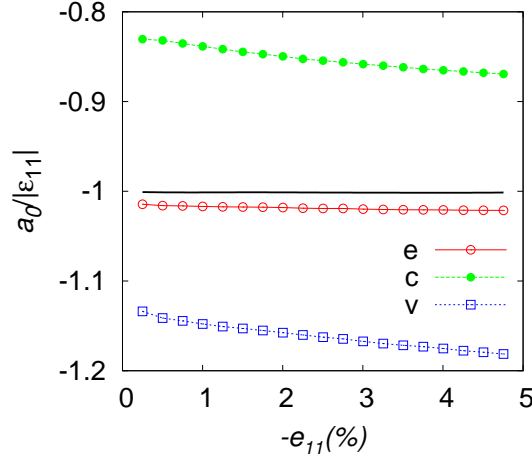
Figure 12: Isotropic loading: evolution of the normalized Fourier components, $a_0/|\varepsilon_{11}|$ of the scaled relative normal displacement $\overline{\Delta u_n}/\langle l \rangle$ for edges (red dots), contacts (green solid circles) and virtual contacts (blue squares). The solid line represents the uniform-strain prediction. Higher-order Fourier coefficients $a_n^{e,c,v}$ are small (data not shown).

The dimensionless normal component of the relative displacements for edges, contacts and virtual contacts ($\overline{\Delta u_n^{e,c,v}}(\theta)/\langle l \rangle_{e,c,v}$) can be decomposed into a Fourier series, similar to Eq. (11a):

$$\frac{\overline{\Delta u_n^{e,c,v}}(\theta)}{\langle l \rangle_{e,c,v}} \;=\; a_0^{e,c,v} + a_n^{e,c,v} \cos 2\theta + ... \tag{23}$$

Again, for symmetry reasons, there is no term involving $\cos \theta$. Now, it is possible to study the evolution of the Fourier components for the different loading conditions used: isotropic (Fig. 12) and triaxial (Fig. 13) loading. In all cases, only the first two components a_0 and a_n are relevant and higher harmonics contributions can be neglected (data not shown).
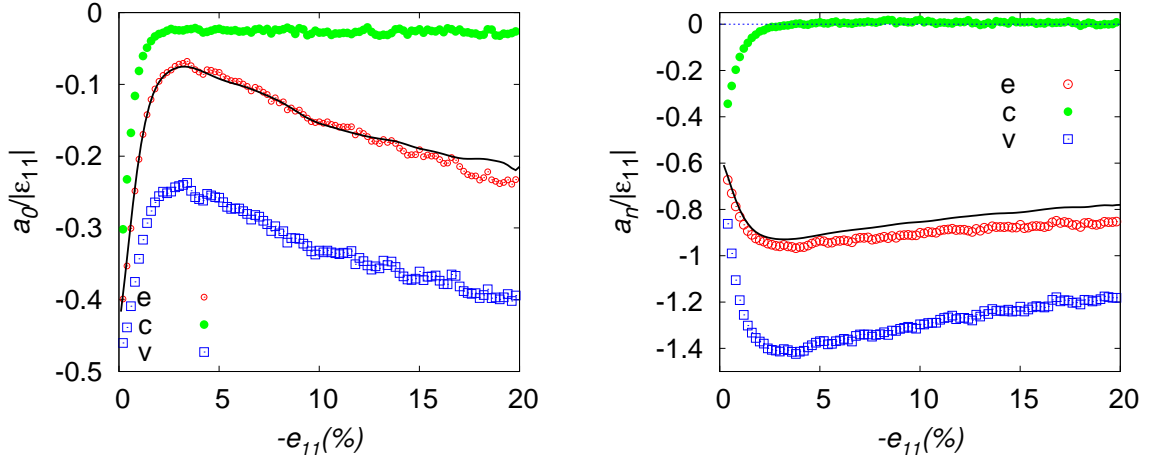
Figure 13: Triaxial loading: evolution of the normalized Fourier components of the scaled relative normal displacement $\overline{\Delta u_n}/\langle l \rangle$) for edges (red circles), contacts (green dots) and virtual contacts (blue squares): (left) $a_0/|\varepsilon_{11}|$ and (right) $a_n/|\varepsilon_{11}|$. The solid line represents the uniform-strain prediction.

The first component $a_0^{e,c,v}$ gives the isotropic contribution to the relative displacement, where negative values mean that the edges/contacts/virtual contacts are compressed. The contacts are, in all cases, compressed less than the edges, while the virtual contacts are compressed more (since there is no repulsive force acting against compression for virtual contacts).

The $a_n^{e,c,v}$ quantify the anisotropic parts, see Eq. (23), where negative values mean that the contacts are compressed in the compressive X-direction, while they are stretched in the perpendicular, azimuthal plane. In particular, for isotropic compression the anisotropic components are all practically zero. For large strain in the triaxial test, the relative displacements of contacts level out at a small, constant value.

While the relative displacements of the contacts saturate at large strains in the triaxial test, the isotropic (anisotropic) Fourier components of edges and virtual contacts increase (decrease) in magnitude.

Somewhat surprisingly, the Fourier components of the normal deformation of edges, $a_{0,n}^e$, nicely follow the uniform-strain predictions $\tilde{a}_0 = (\varepsilon_{11} + \varepsilon_{22})/2$ and $\tilde{a}_n = (\varepsilon_{11} - \varepsilon_{22})/2$, see Eqs. (12a) and (12b). As we will see in the next section, this also applies to the tangential component of the relative displacements. This represents an important characteristic of the

23

deformation of the Delaunay network.

On average, contacts do not deform according to the uniform-strain assumption, contrary to the edges. This is even so for the simple case of isotropic compression (see Fig. 12). For the more complex triaxial loading, contact deformation is only a fraction of the edge deformation (see Fig. 13). In triaxial loading, the Fourier components of the contact deformation become very small at about $e_{11} \approx -2\%$ when the system reaches the yield point (see Fig. 4). Therefore, during what we call the deviatoric regime ($|e_{11}| > 2\%$), the azimuthally-averaged length of contacts does not change (i.e. $\overline{\Delta u}_n^c(\theta) \approx 0$) and thus, using Eq. (22), the normal component of the relative displacement of all edges ($\overline{\Delta u}_n^e(\theta)$) can be approximated in terms of the virtual contact deformation $\overline{\Delta u}_n^v$ as

$$\rho_\theta(\theta)\overline{\Delta u}_n^e(\theta) \approx (1 - n_C)\rho_\theta^v(\theta)\overline{\Delta u}_n^v(\theta) \,, \tag{24}$$

which represents an additional (approximate) normalization condition, valid only in the large strain regime of the triaxial test.

Probability density functions

Probability density functions of relative displacements at contacts have been studied in the two-dimensional case in [Kruyt & Rothenburg, 2003]. Here the probability density functions of edges, (physical) contacts and virtual contacts are given for the normal component of the relative displacement. Figure 14 shows the probability density function of the dimensionless normal deformation $\overline{\Delta u}_n^{e,c,v}/|\varepsilon_{11}|\langle l \rangle_{e,c,v}$ of edges, contacts and virtual contacts for the triaxial loading, along three characteristic directions: $\theta = 0^o$, 45° and 90°.

The range of relative displacements at contacts is narrowly centered at zero, while virtual contacts deform over a much wider range. In both cases, the deformation involves positive and negative contributions (i.e. both extension and compression, respectively). The edge average of the relative normal displacement in the compression direction ($\theta = 0^0$) is negative, in the extension direction ($\theta = 90^0$) it is positive, and in shear direction ($\theta = 45^0$) it vanishes. All this is consistent with the previous observations and with expectation, since positive and negative correspond to compression and tension, respectively.

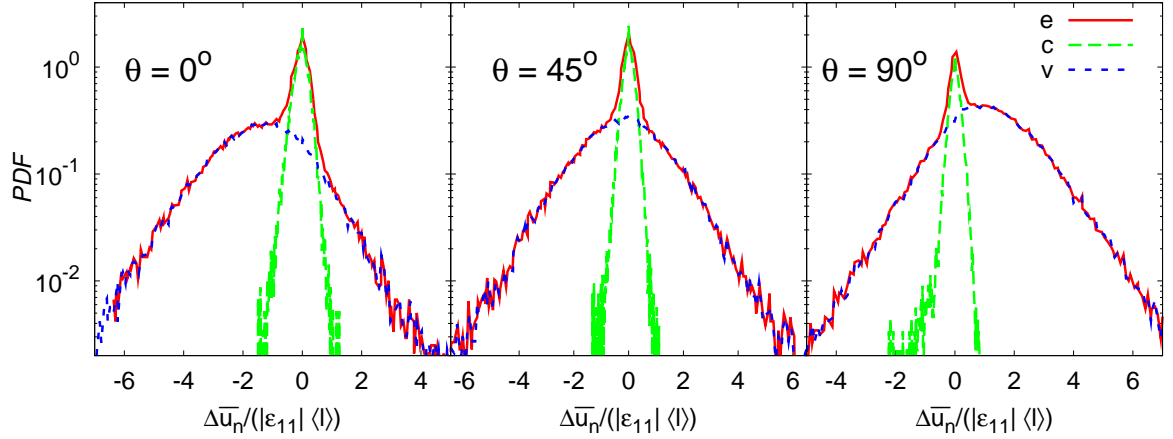Although not shown, similar qualitative behavior is observed for the probability density

Figure 14: Probability density function of $\overline{\Delta u_n}^{e,c,v}/(|\varepsilon_{11}|\langle l\rangle_{e,c,v})$ along three characteristic directions, for the triaxial loading at $e_{11} = -2\%$.

function in isotropic loading. The two main differences are that: (i) the contact normal displacement is virtually truncated at zero, i.e. only very tiny compression at contacts can be achieved, due to the strong repulsive contact forces and (ii) the probability density functions for $\Delta u_n^{c,v}$ are closer to Gaussian distributions (data not shown), while for triaxial loading the probability density functions have near-exponential tails (see Fig. 14).

5.2.2 Tangential component

Fig. 15 shows the polar distribution of the normalized tangential components of the azimuthally-averaged relative displacements $\overline{\Delta u_t}^{e,c,v}/(|\varepsilon_{11}|\langle l\rangle_{e,c,v})$ for edges, contacts and virtual contacts, at different axial deformations e_{11} during triaxial loading.

These averages are well described by a truncated Fourier series, similar to Eq. (11b):

$$\frac{\overline{\Delta u_t}^{e,c,v}(\theta)}{\langle l\rangle_{e,c,v}} \approx -a_t^{e,c,v}\sin 2\theta . \tag{25}$$

The evolution of the Fourier coefficients $a_t^{e,c,v}$ during the triaxial test is plotted in Fig. 16. Similarly to the results for the normal component, the tangential component of the relative displacement of edges closely follows the uniform-strain prediction $\tilde{a}_t = \tilde{a}_n = (\varepsilon_{11} - \varepsilon_{22})/2$, see Eq. (12c). Note that, contrary to the normal components, the tangential (physical) contact displacements are largest, while the edge- and virtual contact displacements are smaller. The edges have approximately the same magnitude of deformation in both normal and tangential

25

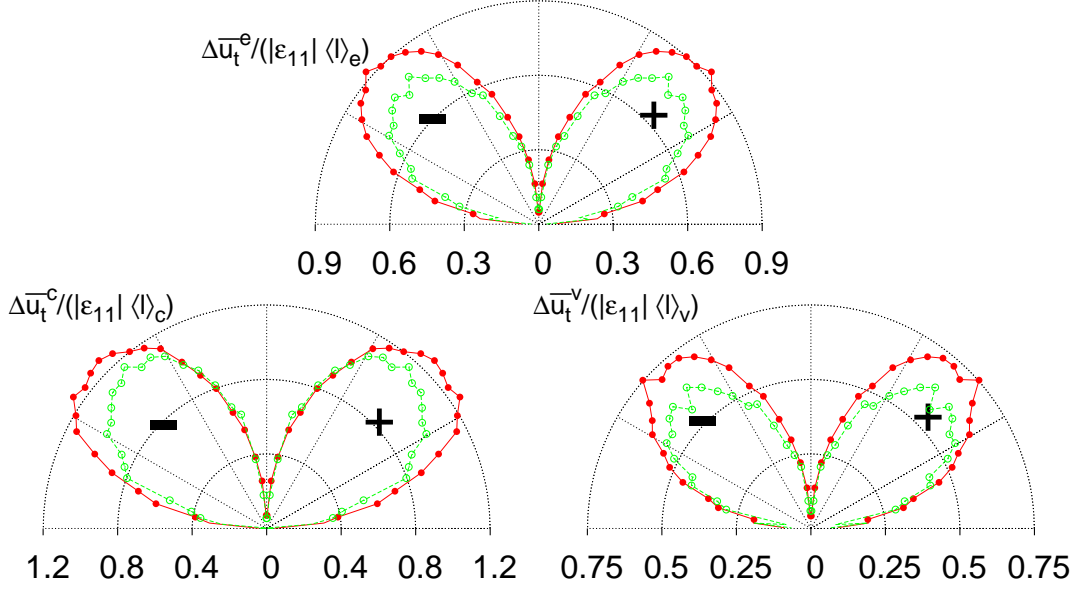direction, since they deform affine, on average (see also Eq. (12c)).

Figure 15: Polar distributions of $\overline{\Delta u}_t(\theta)/(|\varepsilon_{11}|\langle l\rangle)$ at $e_{11} = -2\%$ (•) and -20% (○) for triaxial loading.

Probability density function

Figure 17 shows the probability density function of $\Delta u_t/(|\varepsilon_{11}|l)$ for edges, contacts and virtual contacts for the triaxial test, along three characteristic directions $\theta = 0^o$, 45° and 90°. The probability density functions have near-exponential tails, unlike for isotropic loading, where the distributions are closer to Gaussian (data not shown).

The probability density functions of the out-of-plane component, $\Delta u_s^{e,c,v}$, for edges, contacts and virtual contacts, are qualitatively similar to those of the tangential component $\Delta u_t^{e,c,v}$.

5.3 Deviations from uniform deformation

For development of micro-mechanical constitutive relations, the uniform-strain assumption is often used as the kinematic "localisation assumption" [Cambou et al., 1995]. Here the appropriateness of this assumption is investigated by comparing the orientation-averaged relative displacements with those according to the uniform-strain assumption, Eqs. (12a), (12b) and (12c).
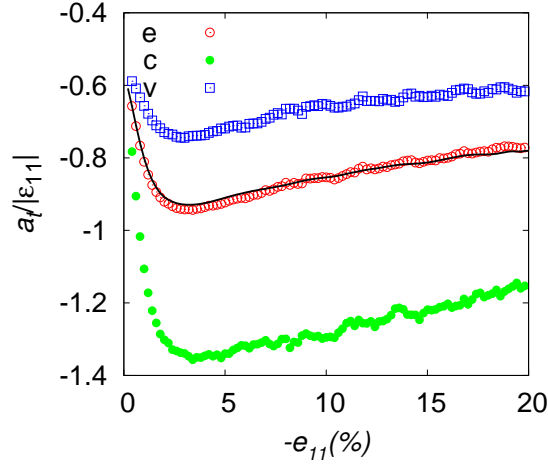
Figure 16: Triaxial loading: evolution of the normalized Fourier components, $a_t/|\varepsilon_{11}|$, of the tangential relative displacements $\overline{\Delta u_t}/\langle l \rangle$ for edges (e: red symbols), contacts (c: green symbols) and virtual contacts (v: blue symbols). The solid line represents the uniform-strain prediction.
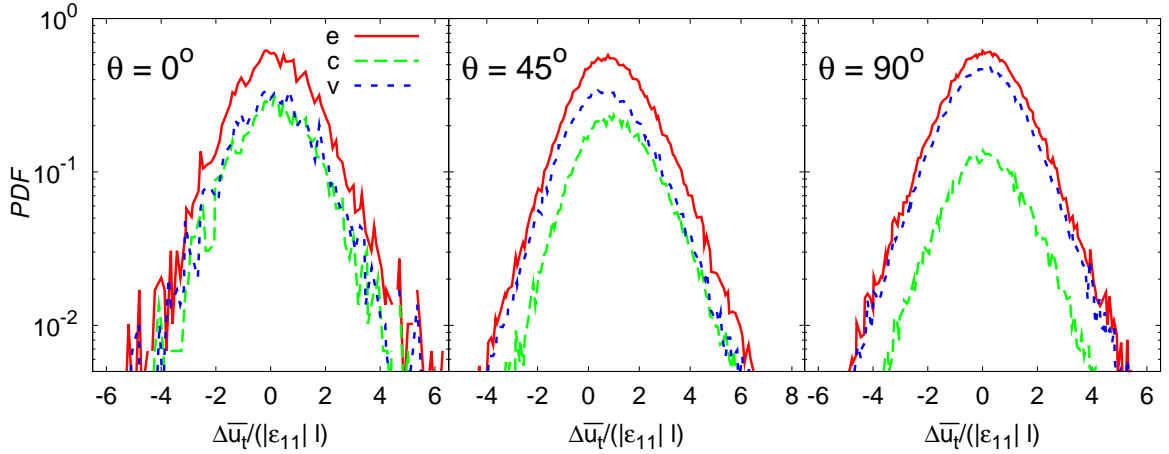

Figure 17: Probability density function of $\overline{\Delta u_t}^{e,c,v}/(|\varepsilon_{11}|\langle l \rangle_{e,c,v})$ for edges, contacts and virtual contacts, along three characteristic directions, during triaxial loading at $e_{11} = -2\%$.

The results of the DEM simulations show that the (azimuthally) averaged relative displacements $\overline{\Delta u_{n,t}}^{e,c,v}(\theta)$ can be expressed as a Fourier series with coefficients $a_{0,n,t}^{e,c,v}$, see Eqs. (23) and (25). Note that the edges' coefficients $a_{0,n,t}^e$ conform to the uniform-strain assumption, while the (physical) contacts and virtual contacts do not behave according to the uniform-strain prediction.

27

The deviations in deformation from the case of uniform-strain (or affine) deformation of edges, contacts and virtual contacts can be characterized by the ratio between the actual Fourier coefficients $(a_{0,n,t}^{e,c,v})$ and those predicted by the uniform strain $(\tilde{a}_{0,n,t})$, i.e. by the set of coefficients:

$$\gamma_{0,n,t}^{e,c,v} \equiv \frac{a_{0,n,t}^{e,c,v}}{\tilde{a}_{0,n,t}} \; . \tag{26}$$

Figure 18 shows the evolution of the set of coefficients $\gamma_{0,n,t}^{e,c,v}$ as function of the imposed deformation, for isotropic and triaxial loading. As was already clear from the previous sections, the deformation of edges follows quite closely the uniform-strain prediction ($\gamma_{0,n,t} \approx 1$), and thus their deformation is on average affine.

In contrast, contact deformation strongly deviates from uniform-strain deformation. The main reason is that the high interparticle stiffness limits the relative displacements of contacts in the normal direction, compared to that of virtual contacts. Therefore, the normal component of the relative displacement of contacts is much smaller than that of edges and of virtual contacts.

For the tangential component, the reverse observation holds to a lesser degree: the deformation of physical contacts and virtual contacts are of the same order of magnitude, but that of physical contacts is larger. Contrary to virtual contacts, the tangential stiffness limits the total deformation of contacts at the contact point, which consists of translational as well as rotational parts. This rotational part will counteract the translational part ('rolling mode of deformation'), i.e. have an opposite sign. This suggests that the tangential component of the relative displacements of contacts is smaller than that according to the uniform-strain assumption.

Thus, the main contribution to the strain arises from the deformation of the voids and from the tangential deformation of contacts.

6   Discussion

Bagi's micro-mechanical formulation [Bagi, 1996] for the strain tensor involves an average over edges of the Delaunay tessellation of relative displacement vectors between particles and the complementary-area vectors. The set of edges can be subdivided into physical contacts and virtual contacts.
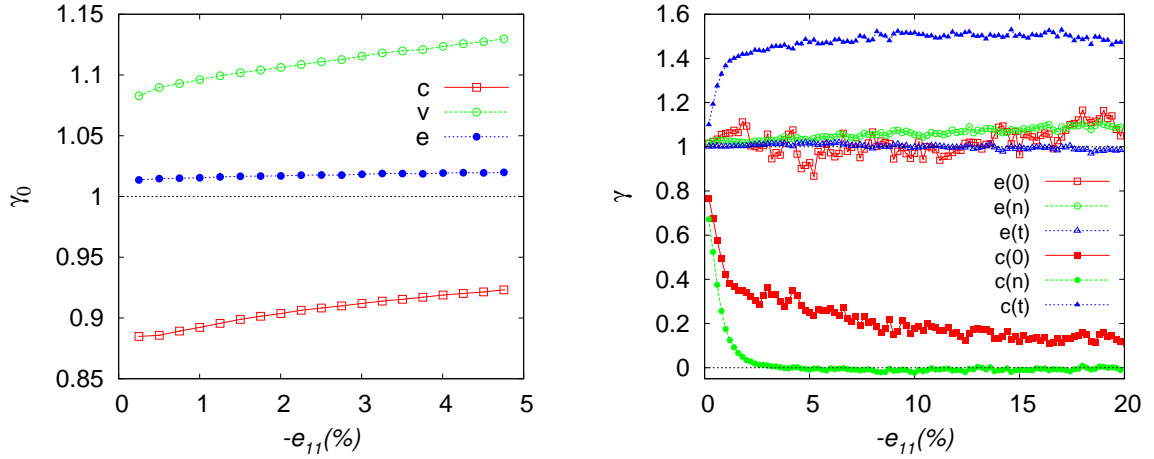
Figure 18: Deviations from the uniform-strain prediction, given by the set of coefficients $\gamma_{0,n,t}^{e,c,v}$ for edges (e), contacts (c) and virtual contacts (v), as function of the axial deformation, for isotropic (left) and triaxial (right) loading. In the former case only the isotropic γ_0 are shown, whereas in the latter case the coefficients for edges (open symbols) and contacts (solid symbols) are shown. Note that symbols like $e(n)$, for instance, have to be interpreted as γ_n^e.

The statistics of: (1) coordination numbers, (2) the edge orientations, (3) the branch vectors, (4) the complementary-area vectors and (5) the relative displacement vectors have been studied here, using results from DEM simulations of isotropic and triaxial compression tests. It is found that:

1. The coordination number for edges is almost constant for the compression and triaxial tests, while the coordination number for contacts shows strong changes.

2. The orientational distribution function of edges is close to isotropic during all tests. The distribution of physical contacts and virtual contacts becomes anisotropic in the triaxial test. All these distribution functions are reasonably well approximated by second-order Fourier series.

3. The average length of the branch vectors of edges and virtual contacts is varying, whereas that of physical contacts is practically constant.

4. The complementary-area vector, on average, only has a non-zero normal component. This average normal component is isotropic for edges and contacts, while that for virtual

contacts shows a mild anisotropy. The average values of the length of the branch vector and the normal component of the complementary-area vector are related to each other and to the volume fraction of the assembly.

5. The orientational averages of the relative displacements for the edges, contacts and virtual contacts are well approximated by second-order Fourier series. The evolution of these Fourier coefficients with imposed strain has been studied and compared to those according to the (averaged) uniform-strain assumption to assess its accuracy.

   The total deformation of the assembly, as given by the orientational averages of the relative displacements of the edges of the Delaunay tessellation follows the uniform-strain prediction. However, neither the deformation of the contact network nor of the virtual contact network has this property. The normal component of the relative displacement of physical contacts is smaller than that according to the uniform-strain assumption, while that of the virtual contacts is larger. The reverse observation holds for the tangential component of the relative displacement vector.

   In isotropic compression the probability density functions for the relative displacements of edges, contacts and virtual contacts are close to Gaussian, while in the triaxial test they exhibit near-exponential tails.

This difference in behavior of the networks of physical and virtual contacts poses a challenge for micro-mechanical modeling. The deformation of the physical contact network, which represents the micro-scale structure of those edges that contribute to the stiffness and thus to the continuum, macro-scale stress, can not easily be predicted. For a micro-mechanical "localisation assumption", an additional relationship between the average deformation of virtual contacts and physical contacts needs to be established, like Eq. (22). The left-hand side of this equation follows from the uniform-strain assumption, so that knowing either $\overline{\Delta u}_{n,t}^{c}(\theta)$ or $\overline{\Delta u}_{n,t}^{v}(\theta)$ would allow one to close the problem by obtaining a "localisation assumption". A possible approach is to investigate, from the DEM results, the interconnection between local contact geometry and local deformation of small clusters of particles. However, this is a topic for future research.

In addition, it is recommended to also consider other loading cases, for example a case where the direction of (initial) anisotropy does not coincide with the direction of loading, as well

30

as other initial conditions, such as a loose initial packing. The Bagi micro-mechanical strain expression, Eq. (3), involves only relative displacements of particle centers, and hence excludes particle rotations. Since this expression is actually for the displacement-gradient tensor, it does describe the continuum-mechanical rotation, i.e. the asymmetrical part of the displacement gradient. The investigation of the role of particle rotations on deformation measures is also a topic for further study.

Acknowledgements

7   Appendix: uniform strain

Here the relative displacement vector according to uniform-strain assumption is expressed in the local, edge-based coordinate system $(\mathbf{n}, \mathbf{t}, \mathbf{s})$ (see Section 3.1) for triaxial loading.

According to the uniform-strain assumption (see Eq. (6)), the relative displacement Δu_i of an edge characterized by the branch vector $l_i \equiv l n_i$ is given by :

$$\Delta u_i = \varepsilon_{ij} l_j \tag{27}$$

with normal and tangential components,

$$\Delta u_n = n_i \varepsilon_{ij} l_j \tag{28a}$$

$$\Delta u_t = t_i \varepsilon_{ij} l_j \tag{28b}$$

$$\Delta u_s = s_i \varepsilon_{ij} l_j \tag{28c}$$

where $\mathbf{t}$ and $\mathbf{s}$ are the tangential edge vectors, defined in Eq. (8).

In the triaxial compression test $\varepsilon_{33} = \varepsilon_{22}$, and hence the strain tensor is given by

$$\varepsilon = \begin{pmatrix} \varepsilon_{11} & 0 & 0 \\ 0 & \varepsilon_{22} & 0 \\ 0 & 0 & \varepsilon_{22} \end{pmatrix} \tag{29}$$

Using Eq. (8), it follows that the orientational-averaged relative displacements (see Section 3) according to uniform strain are given by:

$$\widetilde{\Delta u_n}(\theta, \phi) = \langle l \rangle \left[\left(\frac{\varepsilon_{11} + \varepsilon_{22}}{2} \right) + \left(\frac{\varepsilon_{11} - \varepsilon_{22}}{2} \right) \cos 2\theta \right] \tag{30a}$$

$$\widetilde{\Delta u_t}(\theta, \phi) = -\langle l \rangle \left[\left(\frac{\varepsilon_{11} - \varepsilon_{22}}{2} \right) \sin 2\theta \right] \tag{30b}$$

$$\widetilde{\Delta u_s}(\theta, \phi) = 0 \tag{30c}$$

where the isotropy of the branch vector $||\mathbf{l}(\theta, \phi)|| \approx \langle l \rangle$ has been used (see Section 5.1.3).

References

[Bagi, 1996] Bagi, K. (1996). Stress and strain in granular assemblies. *Mechanics of Materials* 22:165–177.

[Bathurst & Rothenburg, 1988] Bathurst, R.J. & Rothenburg, L. (1988). Micro-mechanical aspects of isotropic granular assemblies with linear contact interactions. *Journal of Applied Mechanics* 55: 17-23.

[Bathurst & Rothenburg, 1990] Bathurst, R.J. & Rothenburg, L. (1990). Observations on stress-force-fabric relationships. *Mechanics of Materials* 9: 65-80.

[Cambou et al., 1995] Cambou, B. & Dubujet, P. & Emeriault, F. & Sidoroff, F. (1995). Homogenization for granular materials. *European Journal of Mechanics A/Solids* 14: 225-276.

[Coppersmith et al., 1996] Coppersmith, S.N. & Liu, C.H. & Majumdar, S. & Narayan, O. & Witten, T.A. (1996). Model for force fluctuations in bead packs. *Physical Review E* 53: 4673–4685.

[Cundall & Strack, 1979] Cundall, P.A. & Strack, O.D.L. (1979). A discrete numerical model for granular assemblies. *Géotechnique* 29: 47–65.

[Durán et al., 2010] Durán, O. & Kruyt, N.P. & Luding, S. (2010). Analysis of three-dimensional micro-mechanical strain formulations for granular materials: evaluation of accuracy. *International Journal of Solids and Structures* 47: 251-260.

[Durán & Luding, 2010] Durán, O. & Luding, S. (2010). Three-dimensional analysis of fabric and stress for polydisperse granular materials. *In preparation*.

[Horne, 1965] Horne, M.R. (1965). The behaviour of an assembly of rotound, rigid, cohesionless particles I and II. *Proceedings of the Royal Society of London A* 286: 62-97.

[Kruyt, 2003a] Kruyt, N.P. (2003). Contact forces in anisotropic frictional granular materials. *International Journal of Solids and Structures* 40: 3537–3556.

[Kruyt & Rothenburg, 2001] Kruyt, N.P. & Rothenburg, L. (2001) Statistics of the elastic behaviour of granular materials. *International Journal of Solids and Structures* 38: 4879-4899.

[Kruyt & Rothenburg, 2002] Kruyt, N.P. & Rothenburg, L. (2002). Probability density functions of contact forces for cohesionless frictional granular materials. *International Journal of Solids and Structures* 39: 571–583.

[Kruyt & Rothenburg, 2003] Kruyt, N.P. & Rothenburg, L. (2003). Statistics of forces and relative displacements at contacts in biaxial deformation of granular materials. In *Proceedings Quasi-static Deformations of Particulate Materials*, pp. 141–150, Budapest, Hungary.

[Kruyt & Rothenburg, 2004] Kruyt, N.P. & Rothenburg, L. (2004). Kinematic and static assumptions for homogenization in micromechanics of granular materials. *Mechanics of Materials* 36: 1157–1173.

[Kruyt & Antony, 2007] Kruyt, N.P. & Antony, S.J. (2007). On force, relative-displacement, and work networks in granular materials subjected to quasi-static deformation. *Physical Review E* 75: 051308.

[Kuhn, 1999] Kuhn, M.R. (1999). Structured deformation in granular materials. *Mechanics of Materials* 31: 407-429.

[Liao et al., 1997] Liao, C.L. & Chang, T.P. & Young, D.H. & Chang, C.S. (1997). Stressstrain relationship for granular materials based on the hypothesis of best fit. *International Journal of Solids and Structures* 34: 4087- 4100.

[Lochmann et al., 2006] Lochmann, K. & Oger, L. & Stoyan, D. (2006). Statistical analysis of random sphere packings with variable radius distribution. *Solid State Sciences* 8: 1397-1413.

[Lovøll et al., 1999] Lovøll, G. & Måløy, K.J. & Flekkøy, E.G. (1999). Force measurements on static granular materials. *Physical Review E* 60: 5872–5876.

[Madadi et al., 2004] Madadi, M. & Tsoungui, O. & Lätzel, M.& Luding, S. (2004). On the fabric tensor of polydisperse granular media in 2D. *International Journal of Solids and Structures* 41: 2563–2580.

[Makse et al., 1999] Makse, H.A. & Gland, N. & Johnson, D.L. & Schwartz, L.M. (1999). Why effective medium theory fails in granular materials. *Physical Review Letters* 83: 5070–5073.

[Metzger, 2004] Metzger, P.T. (2004). Granular contact force density of states and entropy in a modified Edwards ensemble. *Physical Review E* 70: 051303.

[Mueth et al., 1998] Mueth, D.M. & Jaeger, H.M. & Nagel, S.R. (1998). Force distribution in a granular medium. *Physical Review E* 57: 3164–3169.

[Nguyen et al., 2009] Nguyen, N.S. & Magoariec, H. & Cambou, B. & Danescu, A. (2009). Analysis of structure and strain at the meso-scale in 2D granular materials. *International Journal of Solids and Structures* 46: 3257–3271.

[Radjaï et al., 1996] Radjaï, F. & Jean, M. & Moreau, J.J. & Roux, S. (1996). Force distributions in dense two-dimensional granular systems. *Physical Review Letters* 77: 274–277.

[Rothenburg, 1980] Rothenburg, L. (1980). Micromechanics of idealised granular materials. Ph.D. Thesis Department of Civil Engineering, Carleton University, Ottawa, Ontario, Canada.

[Tordesillas et al., 2010] Tordesillas, A. & Walsh, S.D.C. & Muthuswamy, M. (2010). The effect of local kinematics on the local and global deformations of granular systems. *Mathematics and Mechanics of Solids* 15: 3–41.

[van Eerd et al., 2007] van Eerd, A.R.T. & Ellenbroek, W.G. & van Hecke, M. & Snoeijer, J.H. & Vlught, T.J.H (2007). Tail of the contact force distribution in static granular materials *Physical Review E* 75: 060302.